SpezialForschungsBereich F 32

Karl–Franzens Universität Graz
Technische Universität Graz
Medizinische Universität Graz

Infimal Convolution of Total Generalized Variation Functionals for dynamic MRI

M. Schloegl M. Holler A. Schwarzl

K. Bredies R. Stollberger

SFB-Report No. 2016-002 August 2016

A–8010 GRAZ, HEINRICHSTRASSE 36, AUSTRIA

Supported by the
Austrian Science Fund (FWF)

Der Wissenschaftsfonds.

SFB sponsors:

- **Austrian Science Fund** (FWF)
- **University of Graz**
- **Graz University of Technology**
- **Medical University of Graz**
- **Government of Styria**
- **City of Graz**

Magnetic Resonance in Medicine

Infimal Convolution of Total Generalized Variation Functionals for dynamic MRI

Matthias Schloegl[1,2], Martin Holler[2,3], Andreas Schwarzl[1], Kristian Bredies[2,3] and Rudolf Stollberger[1,2,*]

[1]Institute of Medical Engineering, Graz University of Technology, Stremayrgasse 16, 8010 Graz, Austria

[2]BioTechMed-Graz, Graz, Austria

[3]Institute for Mathematics and Scientific Computing, University of Graz, Heinrichstrasse 36, 8010 Graz, Austria

[*]Correspondence to: Rudolf Stollberger,
Graz University of Technology,
Institute of Medical Engineering,
Stremayrgasse 16, A-8010 Graz, Austria.
Phone: +43 316-873-35400.
E-mail: rudolf.stollberger@tugraz.at

Grant sponsor: Austrian Science Fund, Grant number SFB F3209-18 (SFB "Mathematical Optimization and Applications in Biomedical Sciences").

Running Title: ICTGV for dMRI

Number of Words (Abstract) = 197
Number of Words (Body) approximately 4900
Number of Figures: 7
Number of Tables: 3
Number of Citations: 44

Magnetic Resonance in Medicine

ABSTRACT

Purpose: To push the limits in "sub-Nyquist" reconstruction for dynamic MRI applications by means of Infimal Convolution of Total Generalized Variation functionals (ICTGV) regularization.
Theory and Methods: ICTGV comprises a new image prior tailored to dynamic data that achieves regularization via an optimal local balancing between spatial and temporal regularity. In this study it is applied for the first time to the reconstruction of dynamic MRI data. CINE and perfusion scans were investigated to study the influence of time dependent morphology as well as temporal contrast changes. ICTGV regularized reconstruction from the corresponding subsampled MR data is formulated as a convex optimization problem and global solutions are obtained by employing a duality based non-smooth optimization algorithm.
Results: The reconstruction error remain on a low level with acceleration factors up to 16 for both investigated applications. The GPU implementation of the algorithm can be readily applied within the clinical routine.
Conclusion: ICTGV based dMRI reconstruction allows for vast undersampling and therefore enables for very high spatial and temporal resolutions, spatial coverage and reduced scan time. With the proposed distinction of model and regularization parameter it offers a new and robust method of flexible decomposition into components with different degrees of temporal regularity.

Keywords: Dynamic MRI, CMR, Perfusion Imaging, Total Generalized Variation, Infimal Convolution, Variational Models

INTRODUCTION

Dynamic Magnetic Resonance Imaging (dMRI) is an important technique for a broad range of applications from cardiac CINE imaging to dynamic contrast-enhanced (DCE) MRI. It generally aims to visualize time dependent changes of morphology or contrast. A common issue of all dMRI applications is the ultimate trade-off between spatial and temporal resolution. Consequently, dMRI applications benefited strongly from parallel imaging (PI) (1–3) due to the possibility of reducing the number of acquired k-space data. Successful modifications of PI techniques tailored to dMRI were reported in the past (4–8).
In contrast to parallel imaging, improvements based on compressed sensing (CS) (9) techniques are often limited to specific applications. The widely employed temporal Fourier-Transformation (10), for example, is a good choice for periodic dynamics, as for CINE cardiac imaging. However, in the presence of non-periodic motion or contrast dynamics other transforms like Karhunen-Loeve Transform (KLT) (11), temporal PCA (12), temporal derivatives (13) or learned dictionaries (14) may be more efficient. In another work (15) a Wavelet-Transform was employed in the spatial and a Fourier-Transformation in the temporal domain, however, depending on the characteristics of the wavelets, blurring or cartoon-like artifacts are likely to appear. The later artifact was also reported for temporal derivatives in low SNR regime. CS also requires incoherence in the data domain, which can be achieved for MRI by specific modified sampling trajectories for Cartesian (16) or Non-Cartesian (17, 18) data.

A further extension of dynamic CS techniques was carried out with the separation of the dynamic image series into a low rank (L) and a sparse component (S) (19,20). Variations of the such an approach were successfully applied to dMRI reconstruction in (21–23) with an explicit super-positioning of L and S in (24, 25) (L+S). L+S claims to be a natural choice for dynamic data as it models innovations on top of a highly correlated background and is therefore applicable for all kind of dMRI applications. Actually, these models require a *global* and *explicit* separation of dynamic data and background. Such a separation is, however, not generally applicable in particular for spatio-temporal correlations in the intermediate scale. Current works employ a patch-based decomposition to *locally* improve reconstruction quality (26) with increased computational complexity the additional burden of choosing a suitable patch-size.

Variational models for image reconstruction allow to introduce appropriate assumptions on an unknown object which do not necessarily rely on sparsity. Prior knowledge enters in a regularization functional which is weighted against data fidelity. For morphological image reconstruction the Total Generalized Variation (TGV) functional (27, 28), a higher order extension of the well-known Total Variation (TV) functional (29), has been proven to be a favorable image prior in MRI reconstruction (30). By optimally balancing between different orders of differentiation, the TGV functional realizes an image model that enforces linear or polynomial smoothness while still allowing jumps, i.e. sharp boundaries.

While such a model proved to be effective for still images, the question of how to suitably extend such an approach to dynamic data was addressed recently in a general context (31). There, a convex spatio-temporal regularization functional is proposed that optimally balances between (higher order) spatial and temporal regularity by employing an *infimal convolution of differently weighted TGV functionals* (ICTGV). This yields an analytically well-defined and computationally tractable regularization functional that enables the *automatic separation* of a dynamic sequence into components where either *strong spatial* or *strong temporal* regularization is beneficial.

In the present work, the ICTGV-functional is applied for the first time to the reconstruction from highly undersampled dynamic MR-data with different types of application, to further push the limits of "sub-Nyquist" reconstruction.

THEORY

Infimal Convolution of Total Variation Type Functionals

In order to achieve a stable reconstruction method for highly subsampled, noisy dMRI data, we employ spatio-temporal regularization in a variational context: Given a suitable spatio-temporal regularization functional $\mathcal{R}$ and a data fidelity term $\mathcal{D}$ modeling the MR data acquisition process with acquired noisy data d, we aim to reconstruct an image sequence $\hat{u}$ by solving

$$\hat{u} = \arg\min_{u} \mathcal{D}(u, d) + \mathcal{R}(u).$$

Due to undersampling only a small subset of the dMRI data is known. This results in ill-posedness of the image reconstruction problem, and hence the regularization term $\mathcal{R}$ plays a crucial role.

For stationary morphologic images, regularization functionals that enforce piecewise smoothness, such as Total Variation (TV) (29) and Total Generalized Variation (TGV) (27, 28), have been successfully applied to the reconstruction from undersampled MRI data (30, 32).

Our goal is to suitably extend this concept to dynamic data by exploiting temporal correlation. Considering spatio-temporal Total Variation regularization as starting point, a main observation is that the scale of the temporal dimension with respect to the spatial dimensions comprises an additional parameter appearing in spatio-temporal regularization that is not determined by any physical quantity. For TV regularization, this parameter leads a weighting of the temporal derivative and hence defines a trade-off between spatial and temporal regularization. Defining for example

$$\mathrm{TV}_\beta(u) = \| |\nabla u|_\beta \|_1, \quad \text{with} \quad |\nabla u|_\beta = \sqrt{(\partial_x u)^2 + (\partial_y u)^2 + (\beta \partial_t u)^2},$$

the parameter β fixes the space-time scaling and leads to either strong (for large β) or weak (for small β) temporal regularization. As β is not predefined, it can be tuned to adapt the regularization properties. For dMRI datasets its choice, however, would need to fulfill two contradicting requirements: Regions with strong temporal correspondence can be exploited by a large value of β whereas regions with fast movement, such as a quickly beating heart, require a small value to focus on spatial regularity.

The regularization approach proposed in (31) allows to optimally combine these two requirements: Two regularization functionals TV_{β_1} and TV_{β_2} enforcing stronger and weaker temporal regularization, respectively, are combined by *infimal-convolution* (31):

$$\mathrm{ICTV}(u) = \min_v \mathrm{TV}_{\beta_1}(u - v) + \gamma\, \mathrm{TV}_{\beta_2}(v)$$

A main advantage of this approach is that, by choosing an image component v locally between 0 and u, the functional itself optimally balances between stronger and weaker temporal regularization in a local manner. Additionally, this provides a first component $(u - v)$, with less dynamic information due to high temporal regularity, and a second component v, with more dynamic information reflecting low temporal regularity. As we will see, such an optimal balancing comprises a flexible but tailored spatio-temporal regularization approach that benefits from the inherent temporal redundancy of dynamic data and, consequently, allows a high reconstruction quality even in situations with strong undersampling.

To avoid the introduction of staircasing artifacts of TV regularization, we follow the theory provided in (31) and balance between two differently weighted second order spatio temporal TGV functionals. As different weightings of the temporal derivative can, in a more abstract setting, be written as different norms on the gradient and the matrix valued symmetrized derivative, we define the ICTGV regularization functional as

$$\mathrm{ICTGV}^2_{\beta,\gamma}(u) = \min_v \mathrm{TGV}^2_{\beta_1}(u - v) + \gamma\, \mathrm{TGV}^2_{\beta_2}(v), \qquad [1]$$

where

$$\mathrm{TGV}^2_{\beta_i}(u) = \min_w \alpha_1 \||\nabla u - w|_{\beta_{1,i}}\|_1 + \alpha_0 \||\mathcal{E}w|_{\beta_{2,i}}\|_1$$

employs the pointwise norms $|\cdot|_{\beta_{1,i}}$ and $|\cdot|_{\beta_{2,i}}$ on the gradient and symmetrized gradient $\mathcal{E}w = \frac{1}{2}(\nabla w + \nabla w^T)$, respectively. In practice, these norms are chosen such that the functionals focus either on spatial or temporal regularity.

It was shown in (31) that ICTGV yields an analytically well defined convex regularization functional that, in the setting of differently weighting temporal and spatial derivatives, is invariant with respect to translations and rotations in space. Numerically, the solution of ICTGV regularized inverse problems can be carried out with the same techniques as for TV regularization, only the number of variables increases. In particular, in case of a convex data fidelity such as the one resulting from MR modeling, state of the art duality based optimization algorithms can be applied easily and the approximation of globally optimal solutions can be assured.

The application of ICTGV to dynamic MRI

The application of ICTGV regularization for reconstruction of accelerated dynamic MRI amounts to solve the following minimization problem

$$\hat{u} = \arg\min_u \frac{\lambda}{2} \sum_{t,c} \|\mathcal{F}_t(b_c u_t) - d_{t,c}\|_2^2 + \ \mathrm{ICTGV}^2_{\beta,\gamma}(u), \qquad [2]$$

where t enumerates different time frames, c the receiver-coils and $\mathcal{F}_t$ denotes the Fourier operator that accounts for the acquired time dependent samples of the desired magnetization u_t at time t, considering the influence of the coil sensitivity distribution b_c. For non-Cartesian acquisitions a nonuniform Fourier-transform (33) is applied. For the solution of Eq. 2 the coils sensitivities are assumed to be known. In this work they were determined a-priori from the subsampled dataset with an algorithm described in (34). The undersampled measurements of each single coil at time t are denoted with $d_{t,c}$.

Due to normal-distributed noise-characteristics in MRI the data-fidelity term is the L^2 discrepancy. The multiplication of the time-frames $(u_t)_t$ with the sensitivity profiles $(b_c)_c$ is defined pointwise in space.

The minimization problem of Eq. 2 is non-smooth but convex and can be solved by a first order duality based method (35) that results in a rather simple but efficient implementation (see Section "Discretization and Numerical Solution", resp. Appendix).

Model and regularization parameters

Variational methods use a *regularization parameter*, denoted by λ in Eq. 2, that weights data fidelity versus regularization and should be chosen according to the expected noise level. In addition to that, the proposed regularization functional encompasses several weighting parameters that define a model of the expected image structure (*model parameters*).

The parametrization of the regularization functional is performed in a way that a variation of the model parameter does not influence the overall trade-off between regularization and data fidelity. Hence the model parameters must be learned only once for an expected image structure, e.g. CINE cardiac imaging, and remain afterwards unaffected from the noise level and subsampling ratio of subsequent measurements.

Model parameters: A first parameter that is inherent to TGV regularization is the ratio $\frac{\alpha_1}{\alpha_0}$ that defines the weighting of the different orders of differentiation. Previous TGV imaging applications and studies found that fixing this ratio to $\frac{1}{\sqrt{2}}$ yields a robust choice $(30, 36)$, which is hence used throughout this work.

Now rewriting the ICTGV functional as

$$\mathrm{ICTGV}_{\beta,\gamma}(u) = \min_{v} \gamma_1(s)\,\mathrm{TGV}^2_{\beta(t_1)}(u-v) + \gamma_2(s)\,\mathrm{TGV}^2_{\beta(t_2)}(v) \qquad [3]$$

we note that three additional parameters remain to be fixed: $s \in [0,1]$ defines the weights $\gamma_i(s)$ of the first and the second TGV functional and the $t_i \in (0,\infty)$ define two different weightings $\beta(t_1)$, $\beta(t_2)$ of the temporal versus the spatial derivative. The functions $\gamma_i(\cdot)$ are chosen with the intention of not influencing the trade-off between data fidelity and regularization as follows:

$$\gamma_1(s) := \frac{s}{\min(s, 1-s)}, \quad \gamma_2(s) := \frac{1-s}{\min(s, 1-s)} \ .$$

In contrast to a straightforward convex combination as s and $(1-s)$, this ensures that the overall cost of the functional does not reduce to zero as s comes close to zero or one. The smaller of the two factors $\gamma_1(s)$ and $\gamma_2(s)$ always equals one and hence s allows to balance between the $\mathrm{TGV}^2_{\beta(t_i)}$ without reducing or increasing the overall cost of $\mathrm{ICTGV}_{\beta,\gamma}$.

In order to normalize the weighting between spatial and temporal regularization we pursue the following approach: Given weights μ_1 and μ_2 of the spatial and temporal derivative, respectively, we require that integrating the resulting vector norm on the gradient over all possible directions gives the same results as the standard Euclidean norm. This amounts to fix

$$1 = \frac{1}{2\pi} \int_0^{\pi} \int_0^{2\pi} \sqrt{(\mu_1 \sin\theta\cos\varphi)^2 + (\mu_1 \sin\theta \sin\varphi)^2 + (\mu_2 \cos\theta)^2}\, \mathrm{d}\varphi\, \mathrm{d}\theta$$

and provides the spatial and temporal weight as function of their ratio, i.e. $(\mu_1, \mu_2) = \beta(t)$, with $t = \frac{\mu_2}{\mu_1} \in (0,\infty)$ a given ratio.

Regularization parameter: Given a fixed set of model parameters, our method requires only the choice of one regularization parameter. This choice should depend on the signal-to-noise-ratio (SNR), the number of voxels and time frames and the subsampling rate of the MR data. Concerning the later, the cost of the data fidelity term decreases linearly with the subsampling ratio, since the forward operator maps only to sampled data. Based on this observation we define the regularization parameter as a linear function of the subsampling factor r, i.e., $\lambda(r) = kr + d$, and hence need to fix k and d. A further adaption to the noise level an image dimension is possible but omitted for the sake of simplicity.

METHODS

Data Acquisition

The proposed reconstruction technique was applied to CINE cardiac MRI and to non-stress cardiac perfusion imaging. CINE MRI was evaluated with two datasets. One dataset was made available from the ISMRM reconstruction challenge 2014[1] and the second dataset was a retrospectively gated bSSFP short-axis view of a health volunteer measured on 3T scanner (Skyra, Siemens Healthcare, Erlangen, Germany) with the following scan parameters: FOV = 274.62 mm × 340 mm, matrix size = 208 × 168, 25 cardiac phases with a temporal resolution of 42.72 ms, TR/TE/FA = 3.56 ms/1.78 ms/40°, 6 mm slice-thickness, TA=16 s. For reconstruction 30 channels from spine- and body-coil elements were automatically selected.

One dynamic perfusion dataset was made available from New York School of Medicine (NYU). It was acquired in a healthy adult volunteer with a modified Turbo-FLASH pulse sequence on a whole-body 3T scanner (Tim Trio, Siemens Healthcare, Erlangen, Germany) using a 12-element matrix coil array and was already used for evaluation purposes of undersampled dynamic MRI reconstruction in (25).

Different levels of acceleration from 4 to 16 were simulated from the fully-sampled data with poisson-disk sampling for dynamic time-series as proposed in (16). Reconstructions from ICTGV, spatio-temporal TGV, TV and L+S as proposed in (25) were evaluated quantitatively by means of structural-similarity-index (SSIM) (37) and root-mean-squared-error (RMSE) against the Sum-of-Squares (SOS) reconstruction of the fully sampled data. The image reconstruction pipeline for ICTGV, TGV and TV was implemented in C++ with CUDA support using the AGILE library (38). For the L+S reconstruction, the implementation provided at `http://cai2r.net/resources/software` was used.

For ICTGV, a parameter learning as described in more detail below was first carried out on test cases that are different from the ones used in the evaluation. Based on this, parameters were then fixed for CINE and perfusion imaging for all further experiments. A similar parameter learning was also carried out for TGV and TV based reconstruction. In contrast to that, to ensure the best results, the parameters for L+S reconstruction were optimized separately for *each individual case used in the evaluation.* Optimization was carried out on the parameter range as described in (25) and parameters were adapted for each case based on quantitative comparison to the (in practice unknown) ground truth.

The coil sensitivities were estimated with an iterative variational approach from the subsampled data as described in (34).

Parameter learning

The three *model parameters* s, t_1, t_2 as described in Section "Model and regularization parameters" were fixed by evaluating a range of parameter sets with respect to SSIM and RMSE. For CINE cardiac imaging, we used two test cases provided from the ISMRM reconstruction challenge 2014, with different factors of

[1] `http://ismrm.org/challenge/`

undersampling ($r_1 = 5$, $r_2 = 10$), for which a ground truth and a good choice of regularization parameter was known. For cardiac perfusion imaging the parameter training was carried out with the MRXCAT perfusion phantom (39) with a selected slice in mid-ventricular short-axis view, standard settings and additional subsampling of $r = 6$. As a result, the model parameters were fixed as $(t_1, t_2, s) = (4, 0.5, 0.5)$ for CINE cardiac imaging and $(t_1, t_2, s) = (4, 0.5, 0.6423)$ for cardiac perfusion imaging.

The same test cases were also used for regularization parameter learning. Based on the sampling-pattern described in (16), incomplete data was generated for different subsampling rates and the reconstructions for different parameter choices were compared against the ground truth. According to these experiments, final values for k and d were fixed to $(k, d) = (0.34, 4.57)$ for CINE cardiac and $(k, d) = (0.08, 1.56)$ for cardiac perfusion imaging.

An exemplary visualization of our results for parameter tuning is displayed in Figure 1 and Figure 2, respectively. A summary of all relevant parameter choices is given in Table 1. We also remark that, in order to remove a dependency of the regularization parameter from the signal range of the image data, we carried out a normalization to the median of the highest ten percent of the time-averaged reconstruction as preprocessing step.

Discretization and Numerical Solution

We denote by N and M the image space dimensions, by T the number of time-frames, by $U = \mathbb{C}^{N\times M\times T}$ the space of image sequences and by C the number of coils. We define a forward operator mapping from U to the reduced multi-channel dMRI data $d \in \mathbb{C}^{N\times M\times T\times C}$ as

$$K : u \mapsto \left(\mathcal{F}_t \left(b_c u_t\right)\right)_{t,c}, \qquad [4]$$

following the notation defined in Eq. 2. Including the given space-time weights $(\mu_{1,i}, \mu_{2,i}) = \beta_i = \beta(t_i)$ (see Section "Parameter learning") in the differential operators rather than the norms we also define

$$\nabla_{\beta_i} : U \to U^3 \quad \text{and} \quad \mathcal{E}_{\beta_i} : U^3 \to U^6$$

to be a spatio-temporal gradient and spatio-temporal symmetrized gradient operator, respectively. With balancing values $\gamma_i = \gamma_i(s)$, $\|\cdot\|_2$ a discrete L^2 norm and $\|\cdot\|_1$ a discrete L^1 norm employing the standard Euclidean norm pointwise, ICTGV regularized dMRI reconstruction as in Eq. 2 can be re-written as

$$\begin{aligned}\min_{u,v,w_1,w_2} \frac{\lambda}{2}\|Ku - d\|_2^2 + \gamma_1 \left(\alpha_1\|\nabla_{\beta_1}(u - v) - w_1\|_1 + \alpha_0\|\mathcal{E}_{\beta_1} w_1\|_1\right) \\ +\gamma_2 \left(\alpha_1\|\nabla_{\beta_2} v - w_2\|_1 + \alpha_0\|\mathcal{E}_{\beta_2} w_2\|_1\right).\end{aligned} \qquad [5]$$

From an abstract viewpoint Eq. 5 constitutes a convex problem of the form

$$\min_x F(Hx)$$

with H being a linear operator and F a convex, lower semi-continuous functional. Employing convex duality, i.e., that $F(x) = \sup_y (x, y) - F^*(y)$ with F^* denoting the convex conjugate of F, we can further obtain an equivalent saddle-point reformulation as

$$\min_x \max_y \ (Hx, y) - F^*(y).$$

This saddle-point problem is then solved by the primal-dual algorithm of (35) in a way that requires only simple, explicit calculations and that global convergence to an optimal solution is guaranteed. Proper convergence of the algorithm was ensured by computing an approximation of a *duality gap* (36) that is known to be zero only for the optimal solutions. As, according to our experience, 500 iterations are sufficient for the duality gap to indicate a voxel wise error in the range of $\left[10^{-2}, 10^{-5}\right]$, this number of iterations was used for all experiments.

GPU implementation

In order to speed up reconstruction times, the MATLAB prototype was translated to C++/CUDA enabling highly parallel GPU computations. As a consequence, the computational speed was improved drastically with up to 50-fold acceleration. Table 2 summarizes reconstruction times for typical data dimensions and sufficient number of iterations.

RESULTS

Figure 3 shows an ICTGV reconstruction of a CINE cardiac dataset from the ISMRM challenge for different acceleration factors, with the model- and regularization parameters being defined as in Table 1. The reconstructions exhibit a high degree of congruence to the fully-sampled reconstruction with improved noise-suppression in the background up to very high acceleration factors. The reconstruction corresponding to $r = 16$ exhibits more temporal blurring but still poses acceptable reconstruction quality.

Figure 4 shows the same down-sampling experiments for the measured short-axis dataset with an additional comparison to L+S reconstruction. Again the ICTGV reconstruction reaches excellent quality up to $r = 12$ with slightly reduced fidelity for $r = 16$, while L+S based reconstructions exhibit corruption with residual artifacts above reduction factors of $r = 12$. We highlight again, that for L+S the parameters were trained for each acceleration, while for ICTGV one learned parameter set from distinct test cases was used.

Figure 5 displays the results from a down-sampling experiment using perfusion data, where a good delineation of the myocardial wall and the papillary muscles was achieved up to $r = 12$, with reduced temporal fidelity for $r = 12$. For $r = 16$ the reconstruction is corrupted with residual under-sampling artifacts. In comparison to that, the L+S reconstruction yields an acceptable image quality only for acceleration factors $r = 4$ and $r = 8$, with slight corruption of residual aliasing artifacts for $r = 8$ and severe corruption for $r \geq 12$.

Figure 6 displays the ICTGV reconstruction for one of the CINE cardiac datasets and a fixed reduction factor of $r = 8$ together with the computed components that reflect regions admitting more temporal regularity (1st component) and less temporal regularity (2nd component). The later coincides with regions of rapid intensity changes, either caused by blood turbulences or systolic alterations of the heart morphology.
For the perfusion dataset the decomposition into components is shown in Figure 7. Here, the static background, slower contrast dynamics with increased temporal blurring as well as morphologic changes are stored within the first component, while more rapid intensity changes (ventricles) are mapped in the second component. The separation is also displayed by the mean intensity change (magnitude) within the right ventricle (Figure 7b) and myocardium (Figure 7c), where a high agreement of the ICTGV reconstruction to the fully sampled reference is observable.
Finally, a quantitative evaluation by means of SSIM and RMSE against the fully sampled reference as ground-truth is summarized in Table 3. There, ICTGV regularization was compared against spatio-temporal TGV^2_β and TV_β regularization and L+S reconstruction. For fair evaluation, a model and regularization-parameter training as described in Section "Theory" was also carried out both for TGV^2_β and TV_β reconstruction, in particular an optimal weighting of spatial versus temporal differentiation was used. For the L+S reconstruction parameter learning was also carried by means of SSIM and RMSE but, in contrast to ICTGV, TGV^2_β and TV_β, parameters were optimized for each individual test case of the evaluation. Table 3 shows that ICTGV reconstruction almost always scores best for both metrics, with substantial improvement against L+S. For the perfusion case, ICTGV reconstruction also scores considerably better that spatio-temporal TGV^2_β and TV_β.

DISCUSSION

The results presented in this work demonstrate the performance of ICTGV as new spatio-temporal regularization approach for the reconstruction of undersampled dynamic multi-coil MRI data. Two exemplary application scenarios were considered: Cardiac CINE imaging with quasi-periodic morphological motion and cardiac perfusion imaging reflecting contrast changes to due alteration of tissue relaxation properties. The corresponding experiments show the capability of the proposed method to obtain artifact free results with high temporal fidelity and improved noise suppression for both applications up to high acceleration factors. This is also expressed quantitatively in terms of SSIM, RMSE and temporal agreement of the mean contrast variation within the right ventricle and myocardium. The reconstructed images and the time intensity curves indicate a good visualization of both morphological details and temporal dynamics, even for an acceleration factor of 16 for cardiac CINE imaging. This further improves the state-of-the-art of iterative reconstruction methods for undersampled dynamic MRI data. The progress upon the L+S approach, that suffers from a decrease in reconstruction quality for acceleration factors $r \geq 12$, is particularly remarkable since the corresponding parameters were optimized for each individual test case, while for ICTGV, these were fixed

independently of the considered cases beforehand.

Another valuable feature of the presented method is its independence of the a specific motion type such as periodic motion. No application specific assumptions have been made and our test cases show improvements for two quite distinct situations, that have been chosen exemplary for to represent morphological and contrast dynamics.

To assess the benefit of the proposed balancing between spatial and temporal regularization, we have also implemented straightforward spatio-temporal Total Variation and second order Total Generalized Variation regularization (it-self never applied to dynamic MR reconstruction). A quantitative evaluation for different acceleration factors, test cases and error metrics show the superiority of ICTGV in particular for perfusion imaging (Table 3). This improvement can be explained by the observation that rapid intensity changes due to contrast inflow make a decomposition to different scales of temporal regularity even more beneficial.

An additional feature of the presented method is that a decomposition into two components is obtained. For cardiac perfusion imaging slower portions of the intensity changes due to the passing contrast agent, e.g. in the myocardium, and changes in morphology are accumulated in the first component, while regions of fast intensity changes within the ventricles, liver and kidney are depicted by the second component. This has similarities to a decomposition into a temporally component with correlated background (low-rank) and another with temporal changes (sparse). Yet our methods acts *locally*, while the low-rank assumption is inherently global. The local distribution of the image content to the two ICTGV components depends on the model parameters, which were optimized for the overall reconstruction quality. An exploration of ICTGV reconstruction for applications that require a different weighting, e.g. time-resolved MR angiography, where the interest is not the full image, but components with specific contrast dynamics, will be subject to further research.

The presented method clearly distinguishes between model and regularization parameters. The assumption that the former influence the image modeling but are independent of the overall trade-off between regularization and data fidelity has been confirmed by experiments showing that the optimal choice of model parameters is robust along different subsampling rates. For the choice of regularization parameters, the proposed linear adaptation constitutes a heuristic to compensate for alteration of the data-fidelity cost due to subsampling and proved to be effective along a long range of subsampling rates. Experiments for different parameter choices, subsampling rates and error measures further confirmed the linear correlation between subsampling rate and optimal parameter choice. Furthermore, these experiments showed robustness of our method with respect to the regularization parameter choice in the sense that reconstruction quality decreases only slightly for parameter choices within a range of roughly $\lambda = \lambda_{opt} \pm 10\%$ from the optimum (see Figure 2). We point out that the proposed parametrization strategies might be of general interest for other iterative reconstruction approaches, since most state-of-the-art methods depend on different model parameters.

Finally, ICTGV regularized dMRI reconstruction poses a standard non-smooth convex optimization problem that can efficiently be solved with the primal-dual algorithm (35). Due to convexity, it is possible to guarantee

convergence to a global optimum and also to quantify the solution error via a primal-dual gap. The GPU based framework that was developed for this approach performs the whole reconstruction pipeline within a few minutes and is able to handle Cartesian and Non-Cartesian trajectories and the vendor independent ISMRMRD data-format[2].

CONCLUSIONS

The proposed ICTGV-based method constitutes a robust reconstruction framework for highly accelerated dMRI. Our experiments confirm a good visual representation of morphological details as well as contrast dynamics for acceleration factors of 12 and beyond. Consequently, our method addresses clinical demands of reduced scan times, higher spatial and temporal resolutions and spatial coverage and mitigates problems to incomplete breath-hold capabilities or patient compliance. The developed algorithm is able to incorporate promising developments with non-Cartesian sequence design (40, 41). A corresponding GPU accelerated implementation can process the manufacturer independent ISMRMRD data standard completing the whole reconstruction framework within a few minutes and thereby enables the applicability of the proposed method in clinical practice. As additional feature, the method allows a local separation of components beyond the paradigm of background and dynamic information and provides a model of different temporal scales of motion in MRI – a potential that is yet to be explored for specific applications. A future goal will be to extend our approach to volumetric data. While conceptually the method is not limited to any particular space dimension, such an extension will pose additional numerical challenges in terms of computation time and memory requirement and more sophisticated algorithms such as (42, 43) might be necessary to maintain practical applicability.

ACKNOWLEDGMENTS

The authors would like to thank Ricardo Otazo from NYU for providing the cardiac perfusion data, Alexey Samsonov and Sebastian Kozerke for providing the fully sampled data from the ISMRM 2014 reconstruction challenge and Gert and Ursula Reiter from Medical University of Graz for help with data collection and support for evaluation. This work is funded and supported by the Austrian Science Fund (FWF) under grant “SFB F32" (SFB “Mathematical Optimization and Applications in Biomedical Sciences”).

[2] http://ismrmrd.github.io/

APPENDIX: NUMERICAL SOLUTION

As described in Section "Discretization and Numerical Solution", it is our goal to reconstruct an image sequence $u \in U$ by solving

$$\min_{u,v,w_1,w_2} \frac{\lambda}{2}\|Ku-d\|_2^2 + \gamma_1\left(\alpha_1\|\nabla_{\beta_1}(u-v)-w_1\|_1 + \alpha_0\|\mathcal{E}_{\beta_1}w_1\|_1\right) + \gamma_2\left(\alpha_1\|\nabla_{\beta_2}v-w_2\|_1 + \alpha_0\|\mathcal{E}_{\beta_2}w_2\|_1\right),$$

where $\nabla_{\beta_i} : U \to U^3$ and $\mathcal{E}_{\beta_i} : U^3 \to U^6$ are defined as

$$\nabla_{\beta_i} u = (\mu_{1,i}\delta_{x+}u, \mu_{1,i}\delta_{y+}u, \mu_{2,i}\delta_{t+}u)$$

and

$$\mathcal{E}_{\beta_i} v = \left(\mu_{1,i}\delta_{x-}v^1, \mu_{1,i}\delta_{y-}v^2, \mu_{2,i}\delta_{t-}v^3, \frac{\mu_{1,i}\delta_{y-}v^1 + \mu_{1,i}\delta_{x-}v^2}{2}, \frac{\mu_{2,i}\delta_{t-}v^1 + \mu_{1,i}\delta_{x-}v^3}{2}, \frac{\mu_{2,i}\delta_{t-}v^2 + \mu_{1,i}\delta_{y-}v^3}{2}\right).$$

The operators δ_{x+}, δ_{y+}, δ_{t+} and δ_{x-}, δ_{y-}, δ_{t-} define symmetrically extended forward and backward finite difference operators, respectively, with respect to the x, y and t coordinate.
The L^2 norm is defined for $d \in \mathbb{C}^{N\times M\times T\times C}$ as

$$\|d\|_2^2 = \sum_{i,j,t,c} |d_{i,j,t,c}|^2$$

and, abusing notation, the norm $\|\cdot\|_1$ is defined for $v = (v^1, v^2, v^3) \in U^3$ as

$$\|v\|_1 = \sum_{i,j,t} \sqrt{|v^1_{i,j,t}|^2 + |v^2_{i,j,t}|^2 + |v^3_{i,j,t}|^2}$$

and for $w = (w^1, w^2, w^3, w^4, w^5, w^6) \in U^6$ as

$$\|w\|_1 = \sum_{i,j,t} \sqrt{|w^1_{i,j,t}|^2 + |w^2_{i,j,t}|^2 + |w^3_{i,j,t}|^2 + 2|w^4_{i,j,t}|^2 + 2|w^5_{i,j,t}|^2 + 2|w^6_{i,j,t}|^2},$$

where the factor 2 in front of w_4, w_5, w_6 compensates for the symmetrization of the Jacobian in the definition of $\mathcal{E}_{\beta_i}$.
It is our goal to obtain an saddle-point problem of the form

$$\min_x \max_y (Hx, y) - F^*(y)$$

that is equivalent to our original problem. To this aim, first note that ICTGV can be reformulated as

$$\mathrm{ICTGV}^2_{\beta,\gamma}(u) = \min_{x=(u,v,w_1,w_2)} \|H_1 x\|_{1,\alpha,\gamma}$$

with

$$H_1 = \begin{pmatrix} \nabla_{\beta_1} & -\mathrm{Id} & -\nabla_{\beta_1} & 0 \\ 0 & \mathcal{E}_{\beta_1} & 0 & 0 \\ 0 & 0 & \nabla_{\beta_2} & -\mathrm{Id} \\ 0 & 0 & 0 & \mathcal{E}_{\beta_2} \end{pmatrix}, \qquad [6]$$

and

$$\|(p_1, q_1, p_2, q_2)\|_{1,\alpha,\gamma} = \gamma_1 \left(\alpha_1 \|p_1\|_1 + \alpha_0 \|q_1\|_1\right) + \gamma_2 \left(\alpha_1 \|p_2\|_1 + \alpha_0 \|q_2\|_1\right)$$

a weighted L^1 norm. We further need the convex conjugates of $\|\cdot\|_{1,\alpha,\gamma}$ and $\frac{\lambda}{2}\|\cdot - d\|_2^2$ which are given for $z = (p_1, q_1, p_2, q_2)$ as

$$\|z\|_{1,\alpha,\gamma}^* := \sup_{z'} (z, z') - \|z'\|_{1,\alpha,\gamma} = \mathcal{I}_{\{\|\cdot\|_{\infty,\alpha,\gamma} \leq 1\}}(z),$$

where

$$\mathcal{I}_{\{\|\cdot\|_{\infty,\alpha,\gamma} \leq 1\}}(z) = \begin{cases} 0 & \text{if } \max\{\gamma_1\alpha_1\|p_1\|_\infty, \gamma_1\alpha_0\|q_1\|_\infty, \gamma_2\alpha_1\|p_2\|_\infty, \gamma_2\alpha_0\|q_2\|_\infty\} \leq 1, \\ \infty & \text{else,} \end{cases}$$

and

$$(\frac{\lambda}{2}\|\cdot\|_2^2)^*(r) := \sup_{r'} (r, r') - \frac{\lambda}{2}\|r'\|_2^2 = \frac{1}{2\lambda}\|r\|_2^2.$$

Then, an equivalent formulation of Eq. 2 is obtained as

$$\begin{aligned} &\min_u \frac{\lambda}{2}\|Ku - d\|_2^2 + \mathrm{ICTGV}_\beta^2(u) \Leftrightarrow \min_{x=(u,v,w_1,w_2)} \frac{\lambda}{2}\|Ku - d\|_2^2 + \|H_1 x\|_{1,\alpha,\gamma} \\ \Leftrightarrow &\min_{x=(u,v,w_1,w_2)} \max_{y=(z,r)} (Ku, r) - (d, r) - \frac{1}{2\lambda}\|r\|_2^2 + (H_1 x, z) - \mathcal{I}_{\{\|\cdot\|_{\infty,\alpha,\gamma\}} \leq 1}(z) \\ \Leftrightarrow &\min_{x=(u,v,w_1,w_2)} \max_{y=(z,r)} (Hx, y) - (d, r) - \frac{1}{2\lambda}\|r\|_2^2 - \mathcal{I}_{\{\|\cdot\|_{\infty,\alpha,\gamma\}} \leq 1}(z) \\ \Leftrightarrow &\min_{x=(u,v)} \max_{y=(z,r)} (Hx, y) - F^*(y). \end{aligned}$$

with $H = \begin{pmatrix} & H_1 & & \\ K & 0 & 0 & 0 \end{pmatrix}$ and

$$F^*(y) = F^*(z, r) = (d, r) + \frac{1}{2\lambda}\|r\|_2^2 + \mathcal{I}_{\{\|\cdot\|_{\infty,\alpha,\gamma\}} \leq 1}(z),$$

the convex conjugate of $F(y) = F(z, r) = \frac{\lambda}{2}\|r - d\|_2^2 + \|z\|_{1,\gamma,\beta}$.

The last line in the equivalent re-reformulation of Eq. 2 as above now defines a saddle-point problem in a form that can be solved with the primal-dual algorithm as described in (30, 35, 44). The resulting iterations are provided in Algorithm 1. Note that there, instead of using fixed step sizes σ and τ, we employ an adaptive step-size choice as described in (36). The adaptive choice still ensures convergence but potentially allows larger step-sizes and hence a faster method. This is realized by mapping $\mathcal{S}$, which is for $\theta \in (0, 1)$ defined as

$$\mathcal{S}(\sigma\tau, \mathfrak{n}) = \begin{cases} \mathfrak{n} & \text{if } \sqrt{\theta\sigma\tau} \geq \mathfrak{n}, \\ \sqrt{\theta\sigma\tau} & \text{if } \sqrt{\sigma\tau} \geq \mathfrak{n} > \sqrt{\theta\sigma\tau}, \\ \sqrt{\sigma\tau} & \text{else.} \end{cases} \quad [7]$$

The operators P_η, for $\eta > 0$, and P_{L^2} in the algorithm correspond to the proximal mapping of F^* and are defined as

$$P_\eta(\xi)_{i,j,t} = \frac{\xi_{i,j,t}}{\max\left(1, \frac{|\xi_{i,j,t}|}{\eta}\right)} \quad \text{and} \quad P_{L^2}(\xi) = \frac{\xi - \sigma d}{1 + \frac{\sigma}{\lambda}},$$

where, abusing notation, $|\nu|$ is defined as $|\nu| = \sqrt{|\nu^1|^2 + |\nu^2|^2 + |\nu^3|^2}$ for $\nu \in \mathbb{R}^3$ and as $|\nu| = \sqrt{|\nu^1|^2 + |\nu^2|^2 + |\nu^3|^2 + 2|\nu^4|^2 + 2|\nu^5|^2 + 2|\nu^6|^2}$ for $\nu \in \mathbb{R}^6$. The divergence operators $\mathrm{div}^1_{\beta_i}$ and $\mathrm{div}^2_{\beta_i}$ are defined as the negative adjoints of ∇_{β_i} and $\mathcal{E}_{\beta_i}$, respectively.

Initialize: (u, v, w_1, w_2), $(\bar{u}, \bar{v}, \bar{w}_1, \bar{w}_2)$, (p_1, q_1, p_2, q_2, r), $\sigma, \tau > 0$

Iterate:

Dual Update:

$p_1 \leftarrow P_{\gamma_1\alpha_1}\left(p_1 + \sigma\nabla_{\beta_1}(\bar{u} - \bar{v}) - \bar{w}_1\right)$

$q_1 \leftarrow P_{\gamma_1\alpha_0}\left(q_1 + \sigma\mathcal{E}_{\beta_1}\bar{w}_1\right)$

$p_2 \leftarrow P_{\gamma_2\alpha_1}\left(p_2 + \sigma\nabla_{\beta_2}\bar{v} - \bar{w}_2\right)$

$q_2 \leftarrow P_{\gamma_2\alpha_0}\left(q_2 + \sigma\mathcal{E}_{\beta_2}\bar{w}_2\right)$

$r \leftarrow P_{L^2}\left(r + \sigma K\bar{u}\right)$

Primal Update:

$u^+ \leftarrow u - \tau\left(-\mathrm{div}^1_{\beta_1} p_1 + K^* r\right)$

$w_1^+ \leftarrow w_1 - \tau\left(-p_1 - \mathrm{div}^2_{\beta_1} q_1\right)$

$v^+ \leftarrow v - \tau\left(-\mathrm{div}^1_{\beta_1} p_1 - \mathrm{div}^1_{\beta_2} p_2\right)$

$w_2^+ \leftarrow w_2 - \tau\left(-p_2 - \mathrm{div}^2_{\beta_2} q_2\right)$

Stepsize Update:

$\sigma_+ \leftarrow \mathcal{S}\left(\sigma\tau, \frac{\|(u^+, v^+, w_1^+, w_2^+) - (u, v, w_1, w_2)\|_2}{\|H((u^+, v^+, w_1^+, w_2^+) - (u, v, w_1, w_2))\|_2}\right)$

$\tau_+ \leftarrow \sigma_+$

Extrapolation and Update:

$(\bar{u}, \bar{v}, \bar{w}_1, \bar{w}_2) \leftarrow 2(u^+, v^+, w_1^+, w_2^+) - (u, v, w_1, w_2)$

$(u, v, w_1, w_2) \leftarrow (u^+, v^+, w_1^+, w_2^+)$

Algorithm 1: Primal-dual algorithm for solving ICTGV regularized dynamic MR reconstruction.

1. Pruessmann KP, Weiger M, Scheidegger MB, Boesiger P. SENSE: Sensitivity encoding for fast MRI. Magnetic Resonance in Medicine 1999;42(5):952–962.
2. Griswold MA, Jakob PM, Heidemann RM, Nittka M, Jellus V, Wang J, Kiefer B, Haase A. Generalized Autocalibrating Partially Parallel Acquisitions (GRAPPA). Magnetic Resonance in Medicine 2002; 47(6):1202–1210.
3. Stollberger R, Fazekas F. Improved perfusion and tracer kinetic imaging using parallel imaging. Topics in Magnetic Resonance Imaging 2004;15(4):245–254.
4. Kellman P, Epstein FH, McVeigh ER. Adaptive sensitivity encoding incorporating temporal filtering (TSENSE). Magnetic Resonance in Medicine 2001;45(5):846–852.
5. Tsao J. On the UNFOLD method. Magnetic Resonance in Medicine 2002;47(1):202–207.
6. Tsao J, Boesiger P, Pruessmann KP. k-t BLAST and k-t SENSE: Dynamic MRI With High Frame Rate Exploiting Spatiotemporal Correlations. Magnetic Resonance in Medicine 2003;5:1031–1042.
7. Breuer FA, Kellman P, Griswold MA, Jakob PM. Dynamic autocalibrated parallel imaging using temporal GRAPPA (TGRAPPA). Magnetic Resonance in Medicine 2005;53(4):981–985.
8. Huang F, Akao J, Vijayakumar S, Duensing GR, Limkeman M. k-t GRAPPA: A k-space implementation for dynamic MRI with high reduction factor. Magnetic Resonance in Medicine 2005;54(5):1172–1184.
9. Donoho DL. Compressed Sensing. IEEE Transactions on Information Theory 2006;52(4):1289–1306.
10. Otazo R, Kim D, Axel L, Sodickson DK. Combination of compressed sensing and parallel imaging for highly accelerated first-pass cardiac perfusion MRI. Magnetic Resonance in Medicine 2010;64(3):767–776.
11. Jung H, Sung K, Nayak KS, Kim EY, Ye JC. K-t FOCUSS: A general compressed sensing framework for high resolution dynamic MRI. Magnetic Resonance in Medicine 2009;61(1):103–116.
12. Pedersen H, Kozerke S, Ringgaard S, Nehrke K, Kim WY. k-t PCA: Temporally constrained k-t BLAST reconstruction using principal component analysis. Magnetic Resonance in Medicine 2009;62(3):706–716.
13. Feng L, Srichai MB, Lim RP, Harrison A, King W, Adluru G, Dibella EVR, Sodickson DK, Otazo R, Kim D. Highly accelerated real-time cardiac cine MRI using k-t SPARSE-SENSE. Magnetic Resonance in Medicine 2013;70(1):64–74.
14. Wang Y, Ying L, Member S. Compressed Sensing Dynamic Cardiac Cine MRI Using Learned Spatiotemporal Dictionary. IEEE Transactions on Biomedical Engineering 2014;61(4):1109–1120.
15. Lustig M, Santos JM, Donoho DL, Pauly JM. k-t SPARSE: High frame rate dynamic MRI exploiting spatio-temporal sparsity. In Proceedings of the 14th Annual Meeting of ISMRM, Seattle. 2006; 2420.
16. Rizwan A, Xue H, Giri S, Ding Y, Craft J, Simonetti OP. Variable density incoherent spatiotemporal acquisition (vista) for highly accelerated cardiac mri. Magnetic Resonance in Medicine 2014;00:00–00.
17. Tsai CM, Nishimura DG. Reduced Aliasing Artifacts Using Variable-Density k-Space Sampling Trajectories. Magnetic Resonance in Medicine 2000;43:452–458.
18. Winkelmann S, Schaeffter T, Koehler T, Eggers H, Doessel O. An optimal radial profile order based on the golden ratio for time-resolved MRI. IEEE Transactions on Medical Imaging 2007;26(1):68–76.

19. Candès EJ, Li X, Ma Y, Wright J. Robust Principal Component Analysis? Journal of the ACM 2011; 58(3):1–37.
20. Ji H, Huang S, Shen Z, Xu Y. Robust Video Restoration by Joint Sparse and Low Rank Matrix Approximation. SIAM Journal on Imaging Sciences 2011;4(4):1122–1142.
21. Lingala SG, Hu Y, Dibella E, Jacob M. Accelerated Dynamic MRI Exploiting Sparsity and Low-Rank Structure: k-t SLR. Transactions on Medical Imaging 2011;30(5):1042–1054.
22. Zhao B, Haldar JP, Christodoulou AG, Zhi-Pei L. Image Reconstruction from Highly Undersampled. (k,t)-Space Data with Joint Partial Separability and Sparsity Constraints. IEEE Transactions on Medical Imaging 2012;31(9):1809–1820.
23. Christodoulou AG, Zhang H, Zhao B, Hitchens T, Ho C, Liang ZP. High-Resolution Cardiovascular MRI by Integrating Parallel Imaging With Low-Rank and Sparse Modeling. IEEE Transactions on Biomedical Engineering 2013;60(11):3083–3092.
24. Gao H, Rapacchi S, Wang D, Moriarty J, Meehan C, Sayre J, Laub G, Finn P, Hu P. Compressed sensing using prior rank, intensity and sparsity model (PRISM): applications in cardiac cine MRI. In Proceedings of the 20th Annual Meeting of ISMRM, Melbourne. 2012; 2242.
25. Otazo R, Candès E, Sodickson DK. Low-rank plus sparse matrix decomposition for accelerated dynamic MRI with separation of background and dynamic components. Magnetic Resonance in Medicine 2015; 73:1125–1136.
26. Ong F, Zhang T, Cheng J, Uecker M, Lustig M. Beyond Low Rank + Sparse: Multi-scale Low Rank Reconstruction for Dynamic Contrast Enhanced Imaging. In Proceedings of the 23th Annual Meeting of ISMRM, Toronto. 2015; 0575.
27. Bredies K, Kunisch K, Pock T. Total Generalized Variation. SIAM Journal on Imaging Sciences 2010; 3(3):492–526.
28. Bredies K, Holler M. Regularization of linear inverse problems with total generalized variation. Journal of Inverse and Ill-Posed Problems 2014;22(6):871–913.
29. Rudin LI, Osher S, Fatemi E. Nonlinear total variation based noise removal algorithms. Journal of Physics D 1992;60:259–268.
30. Knoll F, Bredies K, Pock T, Stollberger R. Second order total generalized variation (TGV) for MRI. Magnetic Resonance in Medicine 2011;65(2):480–491.
31. Holler M, Kunisch K. On Infimal Convolution of TV Type Functionals and Applications to Video and Image Reconstruction. SIAM Journal on Imaging Sciences 2014;7(4):2258–2300.
32. Block KT, Uecker M, Frahm J. Undersampled Radial MRI with Multiple Coils. Iterative Image Reconstruction Using a Total Variation Constraint. Magnetic Resonance in Medicine 2007;57(6):1086–1098.
33. Fessler J, Sutton B. Nonuniform Fast Fourier Transforms Using Min-Max Interpolation. IEEE Transactions on Signal Processing 2003;51(2):560–574.
34. Schloegl M, Holler M, Bredies K, Stollberger R. A Variational Approach for Coil-Sensitivity Estimation

for Undersampled Phase-Sensitive Dynamic MRI Reconstruction. In Proceedings of the 23th Annual Meeting of ISMRM, Toronto. 2015; 3692.

35. Chambolle A, Pock T. A first-order primal-dual algorithm for convex problems with applications to imaging. Journal of Mathemtical Imaging and Vision 2011;40(1):120–145.
36. Bredies K, Holler M. TGV-based framework for variational image decompression, zooming and reconstruction. Part II:Numerics. To appear in SIAM Journal in Imaging Sciences 2015;.
37. Wang Z, Bovik AC, Sheikh HR, Simoncelli EP. Image qualifty assessment: From error visibility to structural similarity. IEEE Transactions on Image Processing 2004;13(4):600–612.
38. Freiberger M, Knoll F, Bredies K, Scharfetter H, Stollberger R. The agile library for image reconstruction in biomedical sciences using graphics card hardware acceleration. Computing in Science and Engineering 2013;15:34–44.
39. Wissman L, Santelli C, Segars WP, Kozerke S. MRXCAT: Realistic numerical phantoms for cardiovascular magnetic resonance. Journal of Cardiovascular Magnetic Resonance 2014;16(1).
40. Chandarana H, Block TK, Rosenkrantz AB, Lim RP, Kim D, Mossa DJ, Babb JS, Kiefer B, Lee VS. Free-breathing radial 3D fat-suppressed T1-weighted gradient echo sequence: a viable alternative for contrast-enhanced liver imaging in patients unable to suspend respiration. Investigative Radiology 2011; 46(10):648–653.
41. Piccini D, Littmann A, Nielles-Vallespin S, Zenge MO. Spiral phyllotaxis: The natural way to construct a 3D radial trajectory in MRI. Magnetic Resonance in Medicine 2011;66(4):1049–1056.
42. Bredies K, Sun H. Preconditioned Douglas-Rachford algorithms for TV and TGV regularized variational imaging problems. Journal of Mathematical Imaging and Vision 2015;52(3):317–344.
43. Bredies K, Sun H. Preconditioned Douglas-Rachford splitting methods for convex-concave saddle-point problems. SIAM Journal on Numerical Analysis 2015;53(1):421–444.
44. Bredies K. Recovering piecewise smooth multichannel images by minimization of convex functionals with total generalized variation penalty. In A Bruhn, T Pock, XC Tai, eds., Efficient Algorithms for Global Optimization Methods in Computer Vision, volume 8293 of *Lecture Notes in Computer Science*. Springer Berlin Heidelberg, 2014; 44–77.

LIST OF FIGURES

- Figure 1: Model parameter evaluation.
- Figure 2: Regularization parameter evaluation.
- Figure 3: ICTGV reconstructions from ascending degrees of artificial under-sampling for the four-chamber view provided by the ISMRM challenge.
- Figure 4: ICTGV and L+S reconstructions from ascending degrees of artificial under-sampling for a bSSFP CINE cardiac short-axis dataset.
- Figure 5: ICTGV and L+S reconstructions from ascending degrees of artificial under-sampling for cardiac perfusion data.
- Figure 6: Fully sampled reference for a CINE cardiac dataset and ICTGV reconstruction from under-sampled data with $r = 8$ together with components.
- Figure 7: Fully sampled reference for a cardiac perfusion dataset and ICTGV reconstruction from undersampled data with $r = 8$ together with components and display of the mean time-evolution of the signal intensity within the left ventricle and the myocardium.

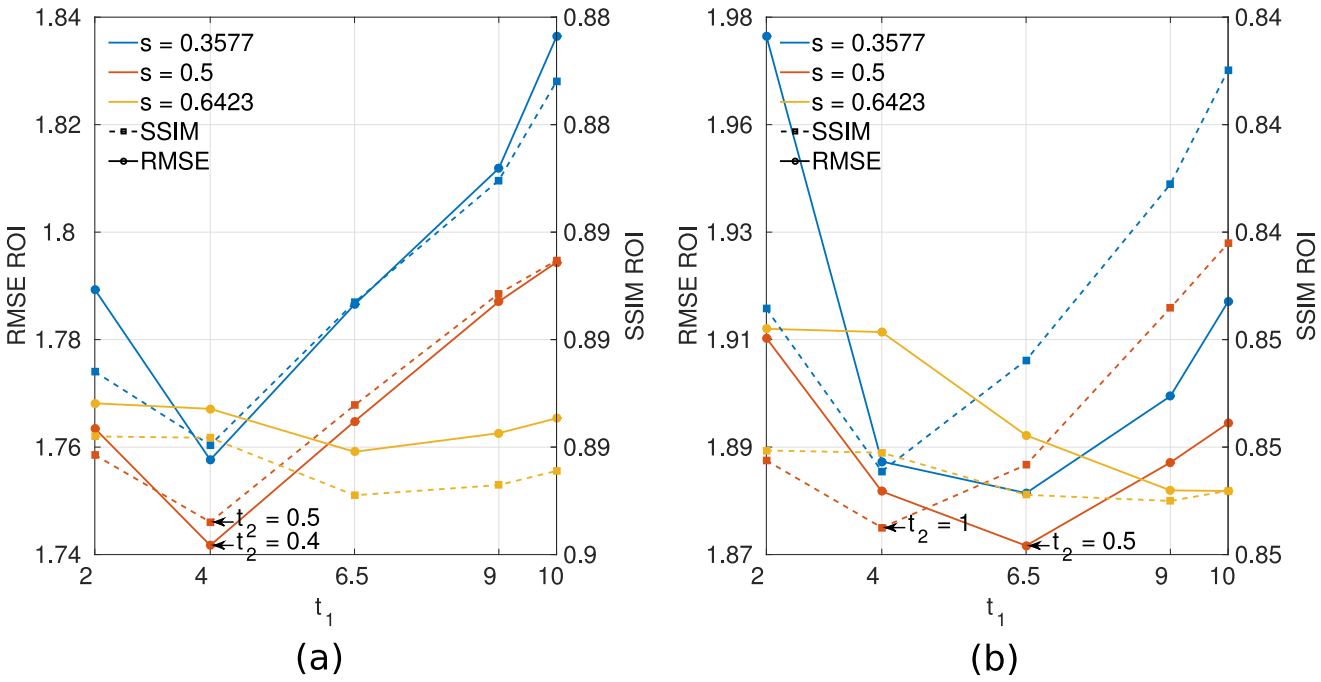

Figure 1: Evaluation of the model parameters s, t_1, t_2 by means of RMSE (solid lines) and SSIM (dashed lines) for a CINE cardiac test-case with acceleration factors $r = 5$ (a) and $r = 10$ (b). The colors indicate three different choices for s. The horizontal axis show different values for t_1 and the vertical axis the corresponding best RMSE and SSIM values achieved with $t_2 \in \{0.2, 0.4, 0.5, 1, 2.5, 3\}$, which are marked (arrow) with the corresponding best value for t_2.

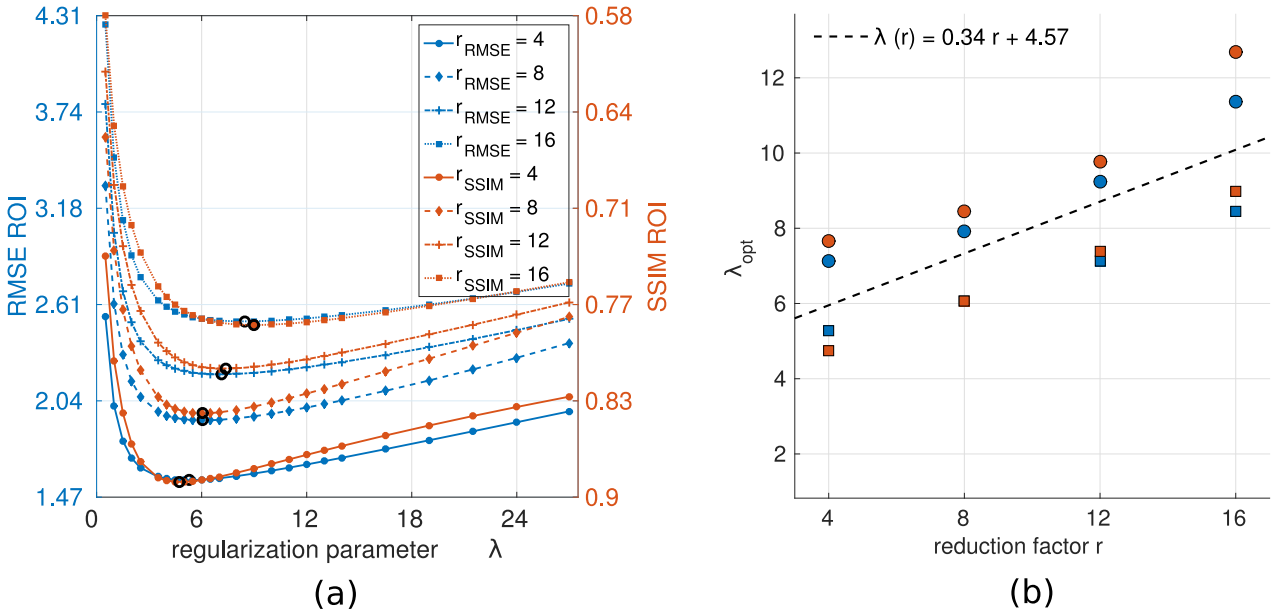

Figure 2: (a) RMSE (blue curves) and SSIM (red curves) evaluation exemplified for one CINE cardiac test case for different regularization parameters λ and acceleration factors $r = 4$ (solid line), $r = 8$ (dashed line), $r = 12$ (dashed-dotted line) and $r = 16$ (dotted line). The corresponding optimal values for λ are indicated with black circles and were calculated by spline-interpolation between the used sample-points. (b) Optimal values for λ according to RMSE (blue) and SSIM (red) for different acceleration factors and the test case displayed in (a) (squares) and the second test case (dots). The linear regression to both cases and metrics (black dashed line) yields the proposed parameter choice.

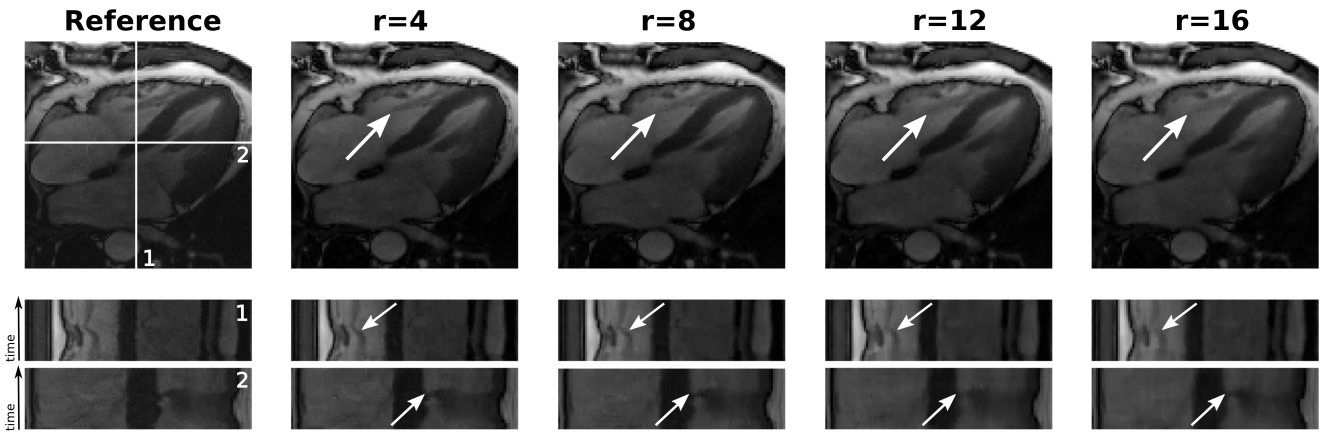

Figure 3: Magnitude images from simulated accelerations $r = (4, 8, 12, 16)$ for the four-chamber-view bSSFP dataset. The fully sampled sum-of-squares reconstruction is display in the 1st column and the therein indicated time-lines are shown in the 2nd and 3rd row.

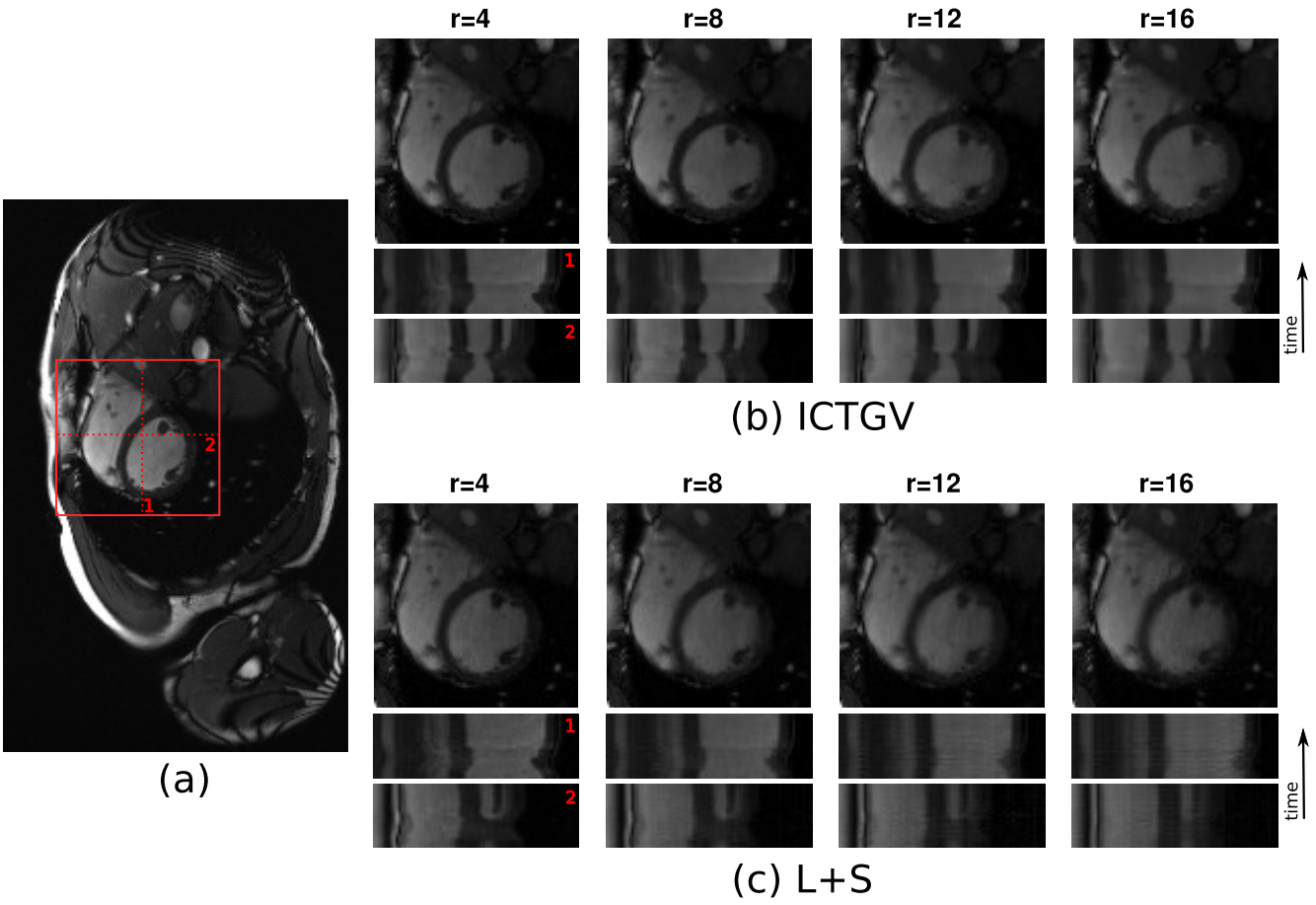

Figure 4: Comparison of ICTGV reconstruction (b) and L+S (c) for retrospectively undersampled bSSFP CINE cardiac data acquired in short-axis-view and undersampling factors ranging from 4 to 16. A late diastolic time-frame of the fully sampled reference reconstruction is displayed in (a) together with an indication of the cropped region and vertical and horizontal time-lines.

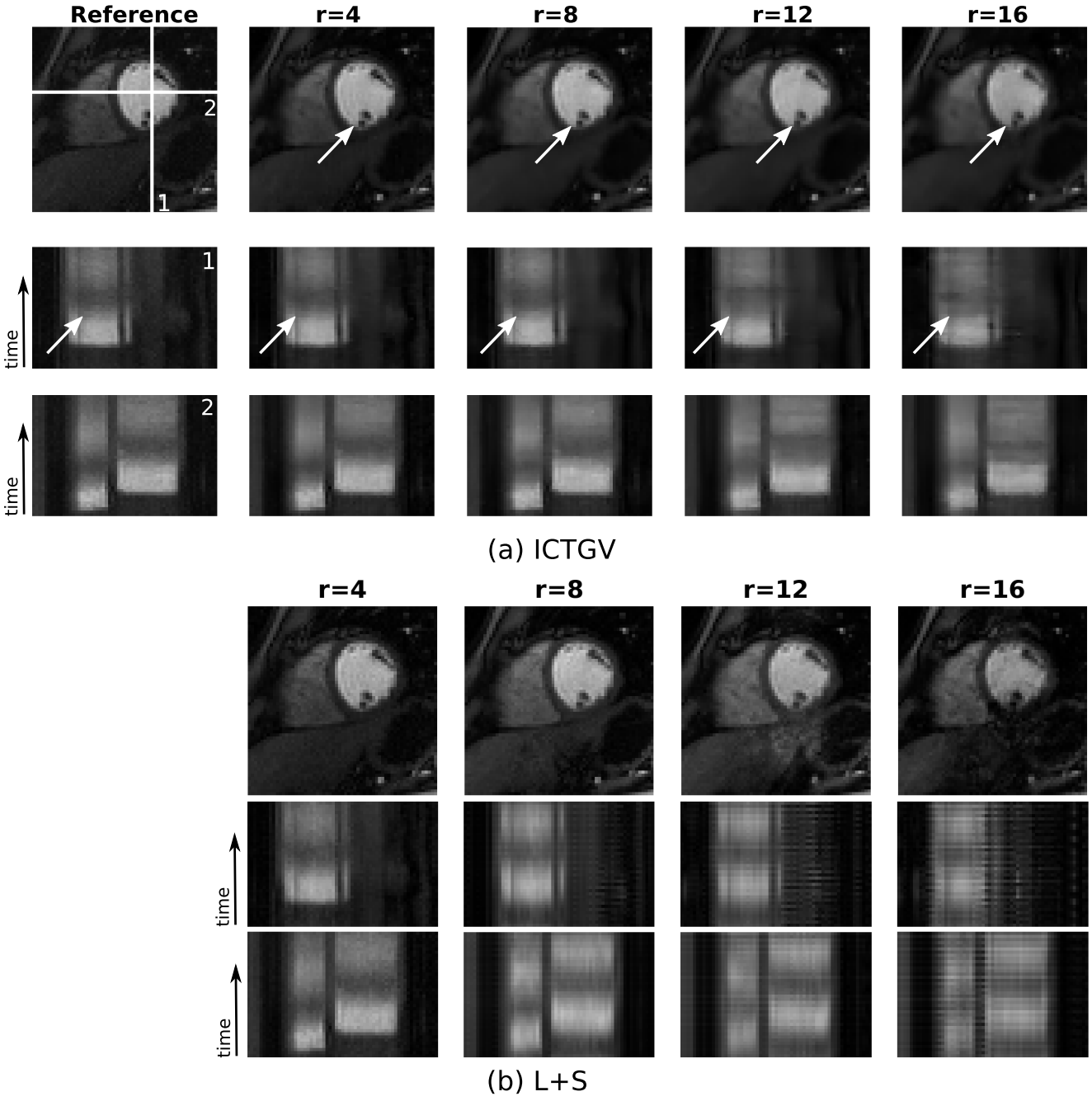

Figure 5: Magnitude images for ICTGV (a) and L+S reconstruction (b) from simulated accelerations $r = (4, 8, 12, 16)$ for the cardiac perfusion dataset. The cropped fully sampled sum-of-squares reconstruction with indicated time-lines is display in the 1st column of (a). The successive columns in (a) and (b) display the reconstructions from the accelerated data for a selected time-frame (1st row) and the corresponding vertical and horizontal time-lines in the 2nd and 3rd row.

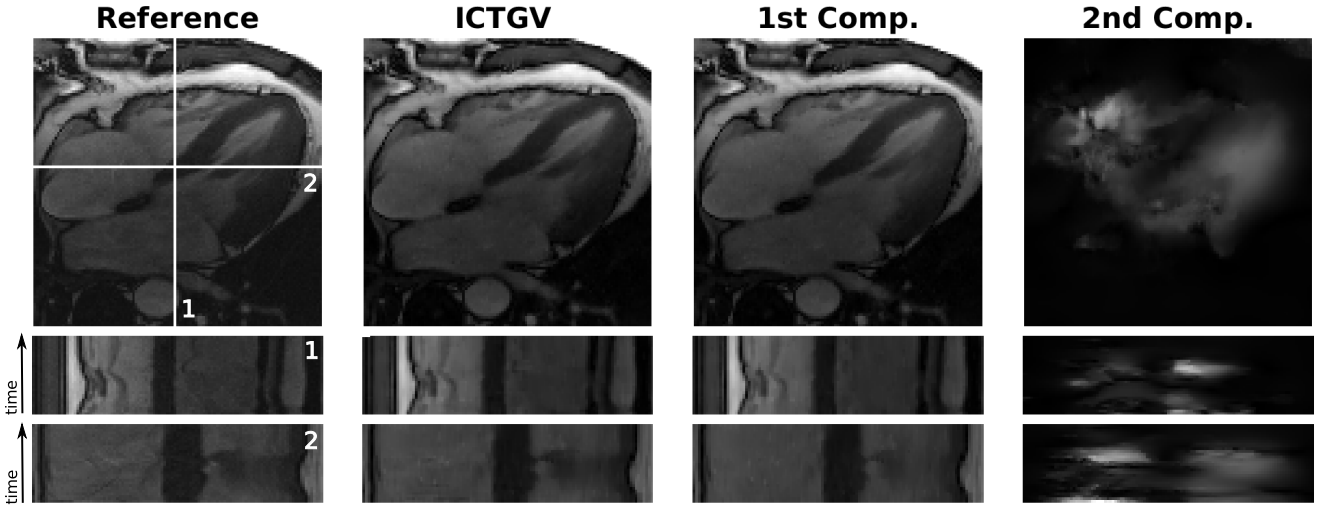

Figure 6: Results for a retrospectively subsampled (r = 8) four-chamber-view CINE cardiac dataset. The top rows show a selected time frame of the fully sampled reference (1st column), ICTGV reconstruction (2nd column), 1st component (3rd column) and 2nd component (4th column). The corresponding time-lines are given in the 2nd and 3rd row. The second component was rescaled for display purposes.

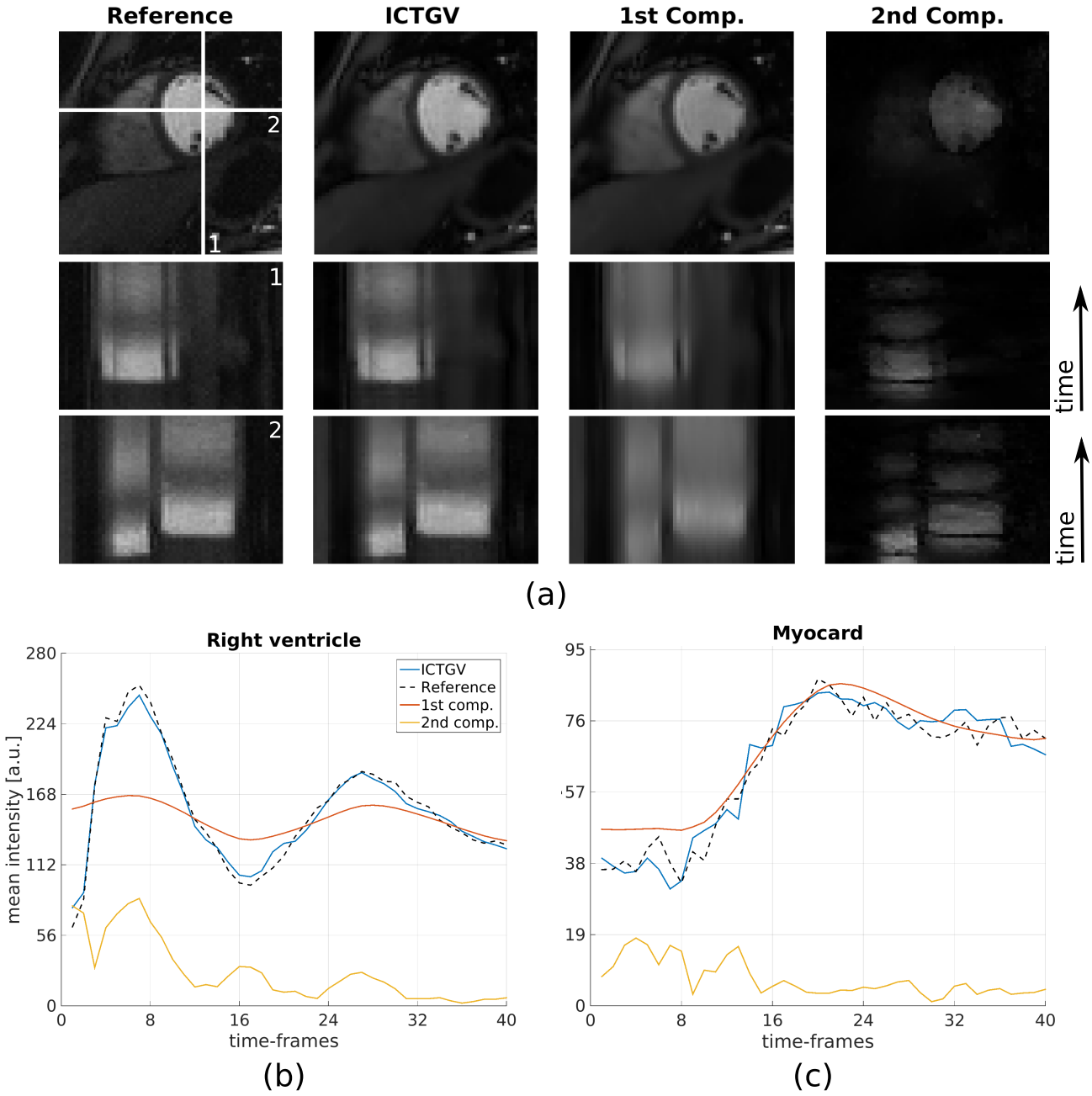

Figure 7: (a) Fully sampled reference (1st column), ICTGV reconstruction (2nd column), 1st component (3rd column) and 2nd component (4th column) for a fixed reduction factor of $r = 8$ and a selected time-frame of a short axis perfusion dataset with the corresponding horizontal and vertical time-lines in the 2nd and 3rd row as indicated in the reference frame. Mean intensity change (magnitude) over time within the right ventricle (b) and the myocardium (c) due to the contrast agent for the reference (black-dotted line), ICTGV reconstruction (blue solid line) and components (red and yellow solid line).The second component was rescaled for display purposes.

LIST OF TABLES

Table 1: Regularization and model parameter choice

Symbol	Denomination	Chosen value		Testing range
Model-parameter		Func.	Perf.	
α_0/α_1	Ratio of TGV weights	$1/\sqrt{2}$	$1/\sqrt{2}$	$--$
$t_1 \to \beta(t_1)$	Spatio-temporal weight 1st comp.	4	4	$[2, 4, 6.5, 9, 10]$
$t_2 \to \beta(t_2)$	Spatio-temporal weight 2nd comp.	0.5	0.5	$[0.2, 0.4, 0.5, 1, 2.5, 3]$
$s \to \gamma_{1,2}(s)$	Weighting between 1st and 2nd comp.	0.5	0.6423	$[0.3577, 0.5, 0.6423]$
Regularization-parameter				
$\lambda(r) = kr + d$	Regularization parameter	$--$		$\lambda \in [0.5, \cdots, 27]$ $r \in [4, 8, 12, 16]$
k	Slope	0.34	0.08	$--$
d	Intercept	4.57	1.56	$--$

Table 2: ICTGV reconstruction times in seconds (500 iterations), obtained with a Matlab CPU implementation (Intel i5-2500K, 3.30GHz) and a Cuda GPU implementation (NVidia GeForce GTX 770), for different data-dimensions (3rd to 5th column) denoted as $(n = N \times M \times T, C)$. The top rows depict the time in seconds to perform 500 iterations while the bottom rows show the total reconstruction time including coil sensitivity estimations.

Device		$(6.553 \times 10^5, 12)$	$(1.747 \times 10^5, 30)$	$(2.328 \times 10^5, 32)$
CPU	Iterations	1325.38	5783.43	8919.39
	Total	1365.86	6238.18	9355.47
GPU	Iterations	34.54	134.34	199.33
	Total	39.73	176.61	244.61

Table 3: Quantitative evaluation (best values underlined) of ICTGV reconstruction against TGV^2_β, TV_β and L+S Reconstruction for artificially down-sampled CINE cardiac and cardiac perfusion cases by means of SSIM and RMSE against the fully sampled sum-of-squares reconstruction.

	ICTGV		TGV^2_β		TV_β		L+S	
	SSIM	RMSE	SSIM	RMSE	SSIM	RMSE	SSIM	RMSE
SA view								
$r = 4$	<u>0.9167</u>	<u>1.2752</u>	0.9164	1.2857	0.9154	1.2892	0.9139	1.37
$r = 8$	0.8739	<u>1.7848</u>	<u>0.8744</u>	1.7952	0.869	1.8272	0.8359	2.429
$r = 12$	<u>0.8376</u>	<u>2.2487</u>	0.8374	2.2665	0.832	2.289	0.7587	3.419
$r = 16$	<u>0.8161</u>	<u>2.5738</u>	0.8147	2.5916	0.8107	2.6003	0.7109	3.96
Four Chamber								
$r = 4$	<u>0.8267</u>	<u>1.8535</u>	0.8227	1.8626	0.822	1.8674	0.77	2.0025
$r = 8$	<u>0.7787</u>	<u>2.1227</u>	0.7726	2.1396	0.7718	2.1541	0.681	2.461
$r = 12$	<u>0.7445</u>	<u>2.3681</u>	0.7399	2.3839	0.7397	2.3907	0.5644	4.2261
$r = 16$	<u>0.7211</u>	<u>2.5619</u>	0.7165	2.5662	0.7154	2.587	0.3862	7.9814
Cardiac Perfusion								
$r = 4$	<u>0.8544</u>	<u>3.0421</u>	0.8169	3.9129	0.7841	4.3812	0.8385	3,353
$r = 8$	<u>0.8162</u>	<u>3.7739</u>	0.7669	4.8956	0.7017	5.8231	0.7024	6.981
$r = 12$	<u>0.7772</u>	<u>4.7878</u>	0.6962	6.331	0.6194	7.3695	0.5859	9.661
$r = 16$	<u>0.7417</u>	<u>5.6376</u>	0.6495	6.8124	0.5668	7.9182	0.4694	11.87